# Al Pinning Effect in Birnessite for High-Performance Ammonium-Ion Storage

*Chao Cheng, Shuyang Bian, Yurong You, Qiang Liu, Zhuoying Yang, Fei Ye, Wenshu Chen, Jun Cheng, Xuecheng Chen, Zilong Tang, Kongjun Zhu, Yuping Wu, and Linfeng Hu**

**Layered birnessite has attracted considerable attention for its cathode potential in various aqueous energy storage devices owing to its two-electron transfer reaction ($Mn^{2+}/Mn^{4+}$), open diffusion channels, and tunable interlayer spacings. However, birnessite for reversible ammonium ($NH_4^+$) ion storage generally suffers from irreversible structural collapse originated from Jahn–Teller (J–T) effect of $Mn^{3+}$ and the intrinsic slow ionic diffusion kinetics. Herein, an Al pinning effect in birnessite is found to address these two issues simultaneously, which promoted enhanced structural stability and resulted in fast ionic diffusion kinetics for excellent high-rate capability. Strikingly, a robust cycling stability over 5, 000 cycles at 1.0 A $g^{-1}$ is achieved in the optimal $Na_{0.7}Al_{0.1}Mn_{0.9}O_2$, which surpasses that of most previously reported ammonium-ion batteries. Density functional theory calculations revealed that the pinned [$Al^{3+}O_6$] octahedra not only decrease the $Mn^{3+}$ content in birnessite, but also strengthen the covalency of Mn—O bonds to resist the collinear elongation/compression direction of the [$Mn^{3+}O_6$] octahedra. Furthermore, Al pinning in birnessite can increase the interlayer spacing due to the regulation of $Mn^{3+}$—O/$Mn^{4+}$—O bond length and decrease the diffusion barrier for $NH_4^+$ ion in the interlayer of birnessite. Thus, an accelerated $NH_4^+$ ion diffusion coefficient of $1.58 \times 10^{-9}$ $cm^2$ $s^{-1}$ has been achieved, which is ≈5 times higher than of the pristine one and also higher than that in other cathode materials. The findings demonstrate that layered $Na_{0.7}Al_{0.1}Mn_{0.9}O_2$ is a very promising cathode candidate for $NH_4^+$ ion battery, and the Al pinning effect in birnessite can effectively suppress the J–T effect and enhance the $NH_4^+$ ion diffusion kinetics simultaneously.**

## 1. Introduction

The rapid development and effective utilization of clean energy sources, such as wind, solar, and geothermal energy, spur the advanced large-scale energy storage systems with a high safety.[1–3] Most recent progress pioneer novel aqueous batteries using non-metallic cations, such as proton ($H^+$), hydronium ($H_3O^+$), halogen anions ($Cl^-$), and ammonium ions ($NH_4^+$), as charge carriers in battery chemistry with the absence of any dendrite growth and corrosion on the anode side.[4–6] Notably, $NH_4^+$ ion displays unique properties as a charge carrier, including a lighter molar mass of 18 g $mol^{-1}$ and a relatively small hydrated ionic radius, which promotes rapid diffusion in aqueous electrolytes.[7] Compared to $H^+$ and $H_3O^+$, $NH_4^+$ ion is less corrosive and shows reduced hydrogen evolution.[8] Given these advantages, aqueous $NH_4^+$ ion batteries (AAIBs) have been considered as the attractive alternatives for next-generation large-scale energy storage systems.[9,10] Unfortunately, the development of AAIBs remains in its infant stage. Up to date, various rare materials have developed as the intercalation-type hosts for $NH_4^+$ ion storage, such as transition metal oxides

---

C. Cheng, S. Bian, Y. You, Q. Liu, W. Chen, L. Hu
School of Materials Science and Engineering
Southeast University
Nanjing 211189, P. R. China
E-mail: linfenghu@seu.edu.cn

Y. Wu, L. Hu
Z Energy Storage Center
Southeast University
Nanjing 211189, P. R. China

Y. Wu
School of Energy and Environment
Southeast University
Nanjing 211189, P. R. China

The ORCID identification number(s) for the author(s) of this article can be found under https://doi.org/10.1002/adma.202512356

**DOI: 10.1002/adma.202512356**

Z. Yang
School of Materials Science and Engineering
Shanghai Jiao Tong University
Shanghai 200240, P. R. China

F. Ye
Nanjing Polytechnic Institute
Nanjing 210044, P. R. China

Z. Tang
State Key Laboratory of New Ceramics and Fine Processing
School of Materials Science and Engineering
Tsinghua University
Beijing 100084, China

K. Zhu
State Key Laboratory of Mechanics and Control for Aerospace Structures
College of Aerospace Engineering
Nanjing University of Aeronautics and Astronautics
Nanjing 210016, P. R. China

(vanadium oxides, manganese oxides, tungsten oxides), Prussian blue analogs (PBAs), and some organic small molecules, covalent organic frameworks (COFs), etc.[11–15] However, none of them combines a high specific capacity, high working voltage, and a robust structure, which are critical for high energy density and long lifespan. Undoubtedly, the main challenge for the advancement of AAIBs remains in the lack of high-performance cathode materials.

Our group previously found very intriguing $NH_4^+$ ion storage performance in inorganic layered compounds, such as $VOPO_4{\cdot}2H_2O$, layered double hydroxides (LDHs), and transition metal carbides ($V_2CT_x$ MXenes) due to their open, large 2D diffusion channels and tunable interlayer spacings.[16–18] These findings induce us to pay more attention to layered birnessite, an important member of the layered manganese oxides. Birnessite generally consists of coplanar layers of edge-shared $[MnO_6]$ octahedra accommodating exchangeable cations and water molecules in the interlayer space.[19,20] Theoretically, birnessite-typed manganese oxides show great promise in $NH_4^+$ ion storage due to their two-electron transfer reaction ($Mn^{2+}/Mn^{4+}$), which provides high specific capacity and a stable operational voltage.[21] However, the $NH_4^+$ ion storage in birnessite generally suffers from Jahn–Teller (J–T) effect of $Mn^{3+}$, which cause structural collapse and manganese dissolution during charge and discharge cycles.[22,23] Various strategies have been developed to address these issues.[24–26] For example, the incorporation of $Mn^{2+}$ into the electrolyte system can successfully reduce manganese dissolution. Unfortunately, the inherent J–T distortion caused by $Mn^{3+}$ ions was not addressed.[27] Additionally, their low intrinsic electrical conductivity and slow diffusion kinetics also present significant obstacles to their electrochemical performance.[28] Carbon coating layers have been used as modification agents for the electrode-electrolyte interface due to their lightweight nature and good conductivity.[29] However, this approach has not effectively alleviated the high strain deformation experienced by manganese-based electrodes during charge and discharge cycles. All of these above-mentioned difficulties should be the reason there is still no any work on the $NH_4^+$ ion storage performance in birnessite series so far.

In the present work, we developed an Al pinning strategy in birnessite, which mitigates theJ–T distortion of $Mn^{3+}$ and simultaneously enhances diffusion kinetics. Both experimental and theoretical investigations revealed that the collinear elongation/compression direction of the $[Mn^{3+}O_6]$ octahedra is restricted by the inert $[AlO_6]$ octahedra. The strategic substitution of $Al^{3+}$ ions effectively curbed the cooperative J-T distortion, enabling its hexagonal phase structure retaining over extended cycling periods (**Scheme** 1). Strikingly, after optimization, the $Na_{0.7}Al_{0.1}Mn_{0.9}O_2$ possesses a specific capacity of 120 mAh $g^{-1}$ at 0.1 A $g^{-1}$ and a capacity retention of 81.6% after 5000 cycles at 1.0 A $g^{-1}$, which surpasses that of most previously reported AAIBs. Furthermore, Al pinning in birnessite can increase the interlayer spacing due to the regulation of $Mn^{3+}$—O/$Mn^{4+}$—O bond length and decrease the diffusion barrier for $NH_4^+$ ion in the interlayer of birnessite, giving rise to a high $NH_4^+$ ion diffusion coefficient of ≈$1.58 \times 10^{-9}$ $cm^2$ $s^{-1}$.

## 2. Results and Discussion

### 2.1. Sample Characterizations

A series of Al-doped P2-$Na_{0.7}Al_xMn_{1\text{-}x}O_2$ samples (where $x$ ranges from 0 to 0.6) were synthesized using the sol–gel method followed by a two-step calcination process (as illustrated in Figure S1, Supporting Information). Powder X-ray diffraction (XRD) peaks of the $Na_{0.7}Al_xMn_{1\text{-}x}O_2$ samples ($x$ = 0.1, 0.2), can be fully indexed as a birnessite-like phase with high crystallinity (hexagonal P2-type structure, S. G. P63/mmc, Figure S2a, Supporting Information). The ICP-OES results in Table S1 (Supporting Information) indicate the chemical compositions of the prepared materials are in good agreement with the initial ratios of reactants. When $x$ value is higher than 0.3, $NaAlO_2$ (JCPDS No. 02-0999) phase with the diffraction peaks at 33.3°, 34.2°, and 34.9° emerged, suggesting the excessive Al doping (Figure S2b, Supporting Information). Rietveld refinement of the solid solution sample was performed to characterize the accommodation sites of Al and Mn ions (**Figures** 1a; S3, Supporting Information). Lattice constant refinement indicates $a$ and $b$ decreased while $c$ parameters increased gradually after Al substitution, as shown in **Table** 1. This occurrence can be ascribed to the smaller ionic radius of $Al^{3+}$ ion (0.535 Å) compared with $Mn^{3+}$ ion (high-spin, 0.645 Å), providing evidence that $Al^{3+}$ ions were successfully incorporated into octahedral Mn sites in the host layers. Co-substitution of $Mn^{3+}$, $Mn^{4+}$ ions by $Al^{3+}$ ion in the birnessite framework gives a charge balance. Rietveld refinement results further demonstrate the decrease of Mn—O bond length while O—Na—O bond length increasing simultaneously (Table 1; Figure S2, Supporting Information). This occurrence can be attributed to a higher covalent Al—O bond energy (509.9 ± 10 kJ $mol^{-1}$) than that of Mn—O bonds (362 ± 25 kJ $mol^{-1}$).[30] As previously revealed by Yang et al., the enhanced TM—O bond strengths in the configuration of O—Na—O—TM—O—Na—O along $c$ axis weaken the O—Na—O bond strengths, leading to the increase of $Na^+$ layer spacing.[31]

X-ray photoelectron spectroscopy (XPS) spectra provide further insights into the influence of doping amount of aluminum on the valence state and bonding environment of manganese. The Mn $2p$ spectrum of $Na_{0.7}Al_xMn_{1\text{-}x}O_2$ ($x$ = 0, 0.1, and 0.2) displayed spin-orbit splitting of the Mn $2p$ orbitals, thereby revealing the Mn $2p^{1/2}$ and Mn $2p^{3/2}$ spin states. The characteristic peaks obtained from spectral fitting are 642.0, 643.1, 653.3, and 654.4 eV, respectively.[32,33] The peaks observed at 642.0 eV (Mn $2p^{3/2}$) and 653.3 eV (Mn $2p^{1/2}$) were attributed to $Mn^{3+}$, while the peaks observed at 643.1 eV (Mn $2p^{3/2}$) and 654.4 eV (Mn $2p^{1/2}$) were attributed to $Mn^{4+}$ (Figure 1c). The XPS results further showed that an increase in aluminum doping led to a gradual decrease in the integrated area of the $Mn^{3+}$ characteristic peaks, while the integrated area of the $Mn^{4+}$ characteristic peaks increased (Figure 1d). This suggests that the concentration of $Mn^{3+}$

---

X. Chen
West Pomeranian University of Technology
Piastow 45, Szczecin 70-310, Poland

J. Cheng
Northwest Institute for Nonferrous Metal Research
Shaanxi Key Laboratory of Biomedical Metal Materials
Xi'an 710016, China

in the samples diminished with the introduction of aluminum, thereby raising the oxidation state of manganese.[34]

Scanning electron microscopy (SEM) and transmission electron microscopy (TEM) images show a 2D bulk morphology with the lateral dimensions ranging from 0.5 to 5.0 µm (Figure 1e,f). Moreover, the selected area electron diffraction (SAED) pattern displayed hexagonally arranged diffraction spots, which can be readily indexed as the in-plane reflections. Energy-dispersive X-ray spectroscopy (EDS) analysis (Figure 1g) demonstrates a homogeneous distribution of Al, Mn, and O elements in each birnessite crystallite. All of these results provide evidence for the successful preparation of high-quality Al-substituted birnessite.

### 2.2. Ammonium Ion Storage Behavior

The $NH_4^+$ ion storage behavior of the Al-substituted birnessite materials, specifically $Na_{0.7}Al_xMn_{1-x}O_2$ ($x = 0$, 0.1, and 0.2), was examined using a Swagelok-typed three-electrode system in a 2.0 M $(NH_4)_2SO_4$ aqueous electrolyte solution. This system comprised a $Na_{0.7}Al_xMn_{1-x}O_2$ working electrode, an active carbon counter electrode, and a saturated Ag/AgCl reference electrode, which has a potential of 0.197 V in relation to the standard hydrogen electrode (SHE). **Figure** 2a illustrates the galvanostatic charge-discharge (GCD) profiles for $Na_{0.7}Al_xMn_{1-x}O_2$ samples, conducted at a current density of 0.1 A $g^{-1}$ within a potential range of −0.2 to 1.0 V (vs Ag/AgCl). The discharge capacity of pristine $Na_{0.7}MnO_2$ is 105.8 mAh $g^{-1}$. After doping, the $Na_{0.7}Al_{0.1}Mn_{0.9}O_2$ sample delivered the optimized performance with a stable discharge voltage plateau at 0.26 V and an impressive specific capacity of 119.3 mAh $g^{-1}$, giving rise to a high energy density (31.2 Wh $kg^{-1}$) superior to mostly cathode materials recently reported (Figure 2b).[35–39] However, an excessive $Al^{3+}$ doping ($x > 0.1$) significantly reduces the specific capacity (80.1 mAh $g^{-1}$ at 0.1 A $g^{-1}$), which should be attributed to the excessive substitution of Al will reduce the content of active Mn atoms. Figure S4 (Supporting Information) displays the cyclic voltammetry (CV) profiles for the optimal $Na_{0.7}Al_{0.1}Mn_{0.9}O_2$ electrode with a voltage range of −0.2–1.0 V. A clear pair of oxidation/reduction peaks was identified at the potential of 0.23 and 0.35 V (vs Ag/AgCl), respectively. TEM images and corresponding EDS mapping results of $Na_{0.7}Al_{0.1}Mn_{0.9}O_2$ cathode at the second charge and discharge states have been provided as shown in Figure S5 (Supporting Information). The EDS elemental maps show apparent decay of the N elements in the charged state, confirming the extraction of $NH_4^+$ ions. The subsequent signal recovery in the discharged state indicates $NH_4^+$ ions re-insertion with a high reversibility.

Notably, the diffusion coefficient of $NH_4^+$ ion ($D_{NH4^+}$) of $Na_{0.7}Al_{0.1}Mn_{0.9}O_2$ determined by the galvanostatic intermittent titration technique (GITT) is $1.58 \times 10^{-9}$ $cm^2$ $s^{-1}$, which is ≈5 times higher than that of $Na_{0.7}MnO_2$ ($3.63 \times 10^{-10}$ $cm^2$ $s^{-1}$) as shown in Figure 2c. The accelerated diffusion kinetic by Al doping promoted superior high-rate capability (Figure 2d). The $Na_{0.7}Al_{0.1}Mn_{0.9}O_2$ electrode delivered a specific capacity of 121.8, 100.1, 82.5, 69.4, 59.4, 53.9 mAh $g^{-1}$ at 0.35, 1.05, 1.75, 3.5, 7.0, 10.5 C, respectively, and remained at 116 mAh $g^{-1}$ when reduced to 0.35 C. The initial coulombic efficiency of 87.31% should be due to the extraction of $Na^+$ ions from the structure during first charging process. In contrast, the pristine $Na_{0.7}MnO_2$ electrode shows a specific capacity of 11.2 mAh $g^{-1}$ at 10.5 C, which is much lower than that of the $Na_{0.7}Al_{0.1}Mn_{0.9}O_2$ sample. Figure S6 (Supporting Information) presents the electrochemical impedance spectroscopy (EIS) spectra of $Na_{0.7}MnO_2$ and $Na_{0.7}Al_{0.1}Mn_{0.9}O_2$ electrodes. Obviously, $Na_{0.7}Al_{0.1}Mn_{0.9}O_2$ electrode has a lower charge transfer resistance of 6.3 Ω than that of pristine $Na_{0.7}MnO_2$ (12.7 Ω), indicating much faster charge transfer. To deeply understand the accelerated $NH_4^+$ ion diffusion kinetics, we simulated the $NH_4^+$ ion diffusion process by density functional theory (DFT)— calculation using the Climbing Image Nudged Elastic Band (CINEB) method.[40] Some simplifications were applied during the calculation with the consideration that $NH_4^+$ ions just diffuse along the voids between the adjacent $[NaO_6]$ trigonal prisms (see Path I and Path II within the *a, b* plane in Figures 2e; S7, Supporting Information). Some $Na^+$ ions were included in this DFT calculation because they are not completely de-intercalated from the birnessite structure during the electrochemical process. Although introducing $Al^{3+}$ into the $[MnO_6]$ octahedron does not change the preferred adsorption sites and transport pathways for $NH_4^+$ ions, the energy barrier for diffusion significantly decreases from 1.57 eV (Path I)/2.42 eV (Path II) in $Na_{0.7}MnO_2$ to 0.74 eV (Path I)/1.98 eV (Path II) upon $Al^{3+}$ incorporation (Figure 2f), which should be the reason of this $NH_4^+$ ion diffusion kinetics enhancement.

Figures 2g and S8 (Supporting Information) show the long-term cycling performance of $Na_{0.7}MnO_2$ and $Na_{0.7}Al_{0.1}Mn_{0.9}O_2$ samples at 0.35 and 3.5 C, respectively. After 100 charge/discharge cycles, the pristine $Na_{0.7}MnO_2$ cathode delivered a drastic capacity decay with only 11% capacity retention after 100 cycles at 0.35 C. In contrast, the $Na_{0.7}Al_{0.1}Mn_{0.9}O_2$ electrode shows a much higher capacity retention of 60% (Figure S8, Supporting Information). Impressively, even after 5000 cycles at a current density of 3.5 C, $Na_{0.7}Al_{0.1}Mn_{0.9}O_2$ sample still exhibited a specific capacity of 52.5 mAh $g^{-1}$ and a capacity retention of 81.6%. Meanwhile, the $Na_{0.7}MnO_2$ electrode only managed 19.5 mAh $g^{-1}$ after 150 cycles (Figure 2g). Figure 2h gives a comparison of the cycling stability in this work with other reported materials. Clearly, the long-term cycling performance of our $Na_{0.7}Al_{0.1}Mn_{0.9}O_2$ surpasses most of the cathode materials previously for AAIBs.[12,16,41–44]

In order to verify the remarkable difference in cycling stability between $Na_{0.7}MnO_2$ and $Na_{0.7}Al_{0.1}Mn_{0.9}O_2$, the content of dissolved manganese ions in the electrolyte was measured by inductively coupled plasma optical emission spectrometry (ICP-OES) after 100 charge/discharge cycles. The concentration of manganese dissolved in the electrolyte of $Na_{0.7}MnO_2$ is 4.8 mg $L^{-1}$ (Figure S9, Supporting Information), while only 1.79 mg $L^{-1}$ was observed in the electrolyte of $Na_{0.7}Al_{0.1}Mn_{0.9}O_2$ cathode, indicating that the manganese dissolution rate is significantly lower than that of the $Na_{0.7}MnO_2$ cathode. SEM observation of the $Na_{0.7}Al_{0.1}Mn_{0.9}O_2$ cathode material after 10 charge/discharge cycles (Figure S10, Supporting Information) confirms the cycled sample well maintains its initial bulk morphology. The corresponding TEM image exhibits well-defined lattice fringes, further confirming the high crystallinity after cycling. However, after 100 charge/discharge cycles, the morphology is gradually changed from 2D microplate to microsphere assembled by abundant wrinkled nanosheets with uniform distribution of Mn, Al, O,

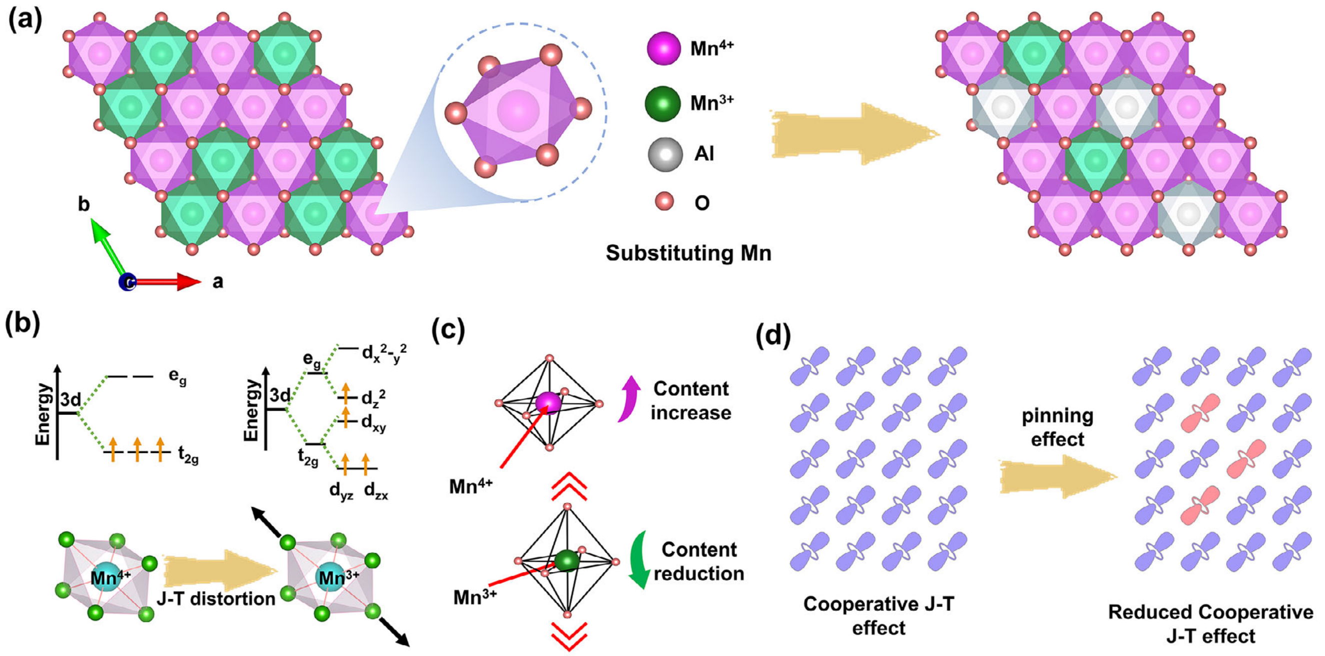

**Scheme 1.** Al ion substitution strategy and its pinning effect. a) Schematic illustration of the Al ion substitution strategy for $Na_{0.7}MnO_2$. b) Splitting of the $e_g$ levels of d orbitals in an octahedral environment caused by the J–T distortion. c) The structure and content changes of $[Mn^{4+}O_6]$ and $[Mn^{3+}O_6]$ octahedra after Al substitution. d) Cooperative J–T distortion with collinear orbital ordering and suppressed J–T distortion after Al pinning.

N and Na elements (Figure S11, Supporting Information). This morphology evolution from a bulk to a sheet-assembly would promote the electrolyte penetration and remarkably facilitate the $NH_4^+$ ion diffusion.

### 2.3. Ammonium-Ion Storage Mechanism

Previous studies have revealed the transport mechanism of tetrahedral-shaped $NH_4^+$ ion has to twist and rotate to maintain a subset of coordinated H-bonds with adjacent oxygen atoms from the crystal host, just like a monkey swinging mechanism.[16] Next, $NH_4^+$ ion storage mechanism of $Na_{0.7}Al_{0.1}Mn_{0.9}O_2$ was carefully studied through ex situ XRD, XPS, and FTIR characterizations. As shown in **Figure** 3a,b, the ex situ XRD patterns exhibit no new peaks during the discharge and charge processes, suggesting that the $Na_{0.7}Al_{0.1}Mn_{0.9}O_2$ cathode still maintains a stable hexagonal crystal structure. An enlarged diffraction peak corresponding to the (002) crystallographic plane is shown in Figure 3c. The (002) peak moved to a smaller angle during the discharge process, from 15.83° (point A, the initial state) to 12.30° (point B, first discharged to 0.1 V). This movement suggests that the insertion of $NH_4^+$ ion was accompanied by the introduction of $H_2O$ into the interlayer, with an interlayer spacing of ≈7.2 Å.[28,45] Furthermore, based on the TG characterization of the sample discharged to point B with a 9.7% quality loss (Figure S12, Supporting Information), its stoichiometric formula can be determined to be $Na_{0.7}Al_{0.1}Mn_{0.9}O_2{\cdot}0.5H_2O$. As the discharge progressed to point C (first fully discharged to −0.2 V), the position of the (002) peak underwent a slight adjustment, changing from 12.30° to 12.14°, indicating further embedding of $NH_4^+$ ion. When charged to 0.5 V (point D), the (002) diffraction peak shifted from 12.14° to 12.22°, along with an increase in peak intensity, suggesting that some of the interlayer $NH_4^+$ ion had been partially removed from the $Na_{0.7}Al_{0.1}Mn_{0.9}O_2$ structure. As the charging voltage increased to 1.0 V, the (002) diffraction peak shifted from 12.22° to 12.28°, indicating the complete extraction of $NH_4^+$ ion from the interlayer spaces. This observation indicates that $Na_{0.7}Al_{0.1}Mn_{0.9}O_2$ exhibited satisfactory reversibility and the storage of $NH_4^+$ ion is likely to occur through a monkey swinging mechanism.

Ex situ Mn 2*p* XPS spectra (Figures 3d,e; S13, Supporting Information) provide additional evidences for $NH_4^+$ ion intercalation/de-intercalation. When the sample underwent the transition from the pristine state A to the fully discharged state of point C (−0.2 V), the intensity of the $Mn^{3+}$ peak at 642.0 eV increased, whereas that of the $Mn^{4+}$ peak at 643.1 eV decreased, suggesting the reduction of $Mn^{4+}$ to $Mn^{3+}$ caused by the intercalation of $NH_4^+$ ion in $Na_{0.7}Al_{0.1}Mn_{0.9}O_2$. On the contrary, during the charging process from the fully discharged state of point C (−0.2 V) to the fully charged state of point E (1.0 V), the intensity of the $Mn^{4+}$ peak increased, while that of the $Mn^{3+}$ peak decreased. During the discharge state from point E (fully charged at 1.0 V) to point G (fully discharged at −0.2 V), the valence state of manganese showed a trend similar to that in the first discharge cycle, indicating that the intercalation and extraction of $NH_4^+$ ion were associated with a reversible transition of the manganese valence state. Figure 3e shows the N 1*s* XPS spectra of $Na_{0.7}Al_{0.1}Mn_{0.9}O_2$ at different discharged and charged states. The peaks at binding energies of 400.0 and 401.4 eV are attributed to the nitrogen atoms in dissociative $NH_4^+$ ion and the nitrogen atoms involved in hydrogen bonding, respectively.[46] A new peak

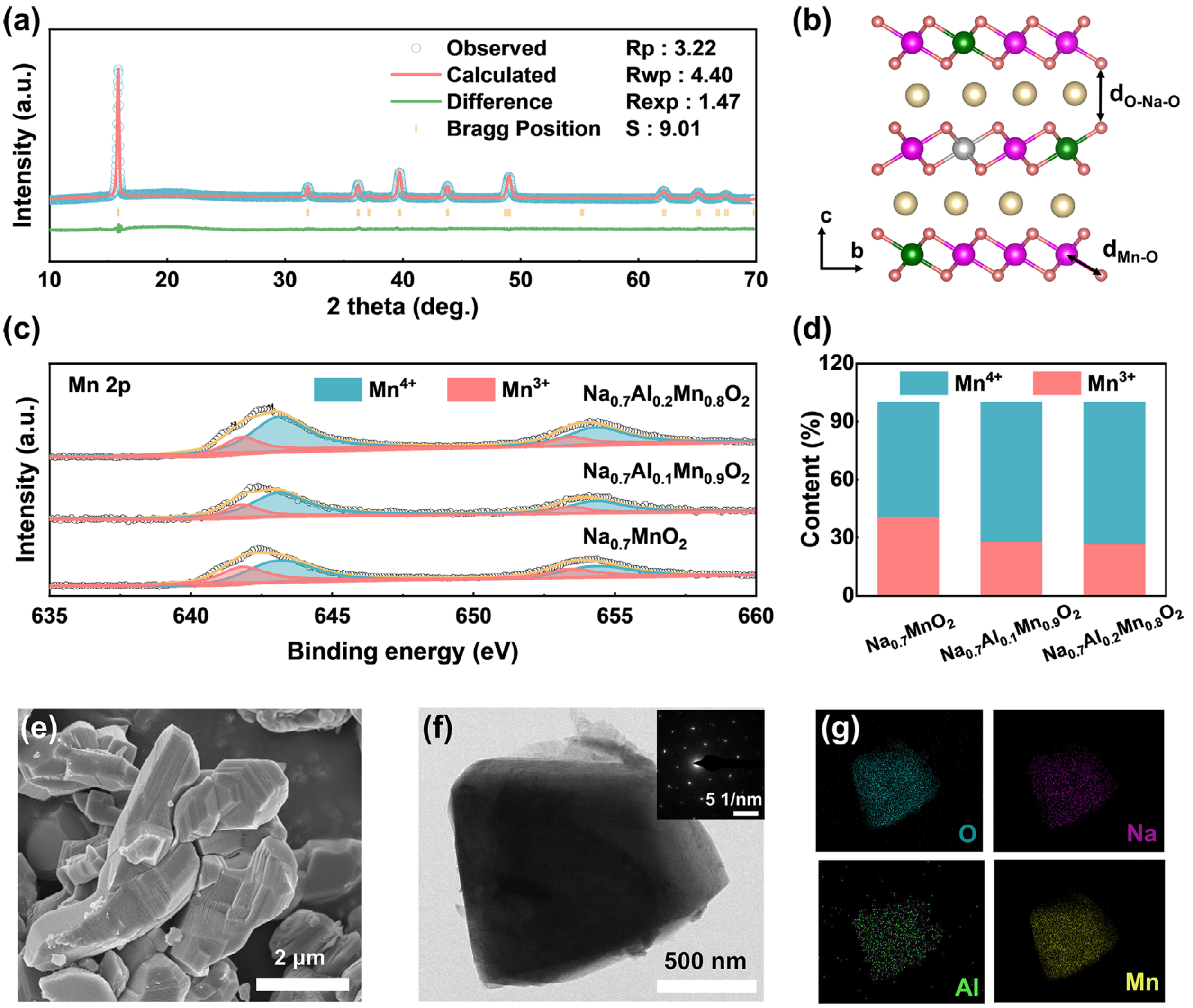

**Figure 1.** Synthesis and characterization of the Al-substituted birnessite. a) Rietveld refinement of the XRD pattern of $Na_{0.7}Al_{0.1}Mn_{0.9}O_2$. b) Schematic illustration of Mn—O, O—Na—O bond in the birnessite structure. c) Mn *2p* XPS spectra and d) the deconvolution results of $Mn^{3+}$ and $Mn^{4+}$ proportions in the samples of $Na_{0.7}Al_xMn_{1-x}O_2$ ($x = 0$, 0.1, and 0.2). e) SEM image, f) TEM image with inserted SAED pattern, g) EDS mapping results of the prepared $Na_{0.7}Al_{0.1}Mn_{0.9}O_2$ material.

—N—H— at 401.8 eV emerged and its intensity increased gradually from the discharged state B to the fully discharged state C, suggesting the intercalation of $NH_4^+$ ion into the lattice of $Na_{0.7}Al_{0.1}Mn_{0.9}O_2$ during the discharge process.[47] The intensity of the —N—H— peak decreased when the system was charged from the point C to point E, while increased again during the following discharge process from the point E to point F, revealing highly reversible intercalation and extraction of $NH_4^+$ ion in the $Na_{0.7}Al_{0.1}Mn_{0.9}O_2$ cathode.

Hydrogen bond formation throughout the $NH_4^+$ ion intercalation and extraction cycling process was further substantiated via ex situ Fourier transform infrared spectroscopy (FTIR) analysis (Figure S14, Supporting Information). The N—H vibrations in $NH_4^+$ ion exhibit two distinctive peaks approximately at 2880 and 3000 $cm^{-1}$. The former peak corresponds to the N—H stretching vibration, suggesting the creation of a hydrogen bond with the Mn—O host, while the latter pertains to the N—H stretching vibration in non-bonding hydrogen.[48] The intensity of these peaks gradually increases from state A to state C, implying that $NH_4^+$ ion are intercalated into the cathode via bonding with the Mn—O host involving hydrogen atoms. The peak intensity subsequently diminishes from state C to state E due to the disruption of

**Table 1.** Refined lattice parameters and Mn—O, Na—O—Na bond lengths of Al-substituted birnessite.

| $Na_{0.7}Al_xMn_{1-x}O_2$ | $x = 0$ | $x = 0.1$ | $x = 0.2$ |
|---|---|---|---|
| $a = b$ (Å) | 2.866(2) | 2.825(5) | 2.798(3) |
| $c$ (Å) | 11.221(1) | 11.281(2) | 11.304(3) |
| $V$ (Å$^3$) | 80.221(7) | 80.752(4) | 81.032(6) |
| $d_{Mn-O}$ (Å) | 1.975(3) | 1.931(4) | 1.922(6) |
| $d_{Na-O-Na}$ (Å) | 3.322(2) | 3.532(5) | 3.612(2) |

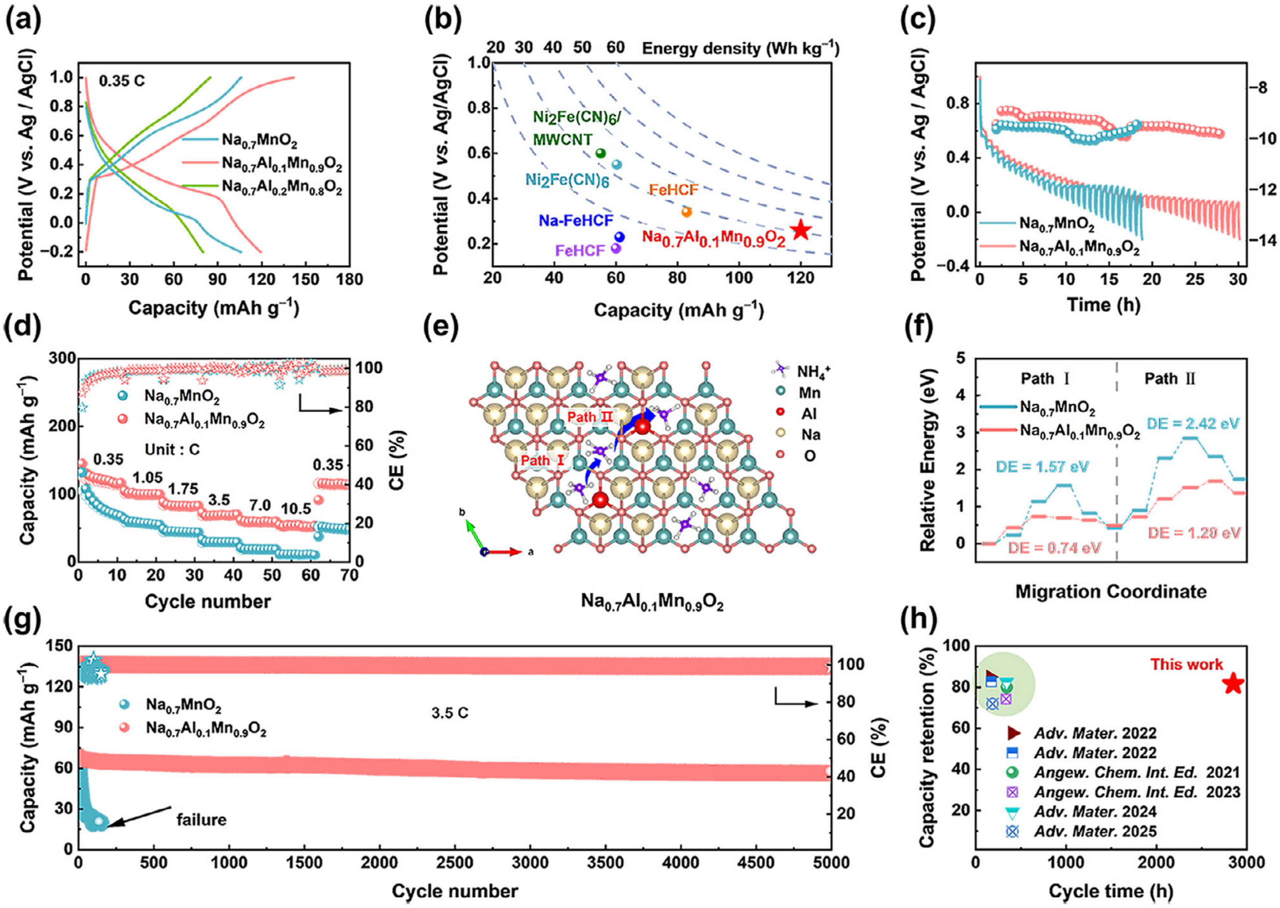

**Figure 2.** Ammonium ion storage performance. a) GCD profiles of $Na_{0.7}Al_xMn_{1-x}O_2$ (x = 0, 0.1, and 0.2) samples at 0.35 C in the 2.0 M $(NH_4)_2SO_4$ electrolyte. b) A comparison of the discharge voltage plateaus and specific capacities between our $Na_{0.7}Al_{0.1}Mn_{0.9}O_2$ sample and some previously reported representative cathodes for AAIBs.[35–39] c) GITT profiles and the associated $NH_4^+$ ion diffusion coefficients for $Na_{0.7}MnO_2$ and $Na_{0.7}Al_{0.1}Mn_{0.9}O_2$ cathodes. d) Rate performance of $Na_{0.7}MnO_2$ and $Na_{0.7}Al_{0.1}Mn_{0.9}O_2$ samples. e) The side view of the schematic illustration depicts the two $NH_4^+$ ion diffusion pathways (Path I and Path II) and f) the associated diffusion barrier profiles for $Na_{0.7}Al_{0.1}Mn_{0.9}O_2$ along the ab plane. g) Long-term cycling performance of $Na_{0.7}MnO_2$ and $Na_{0.7}Al_{0.1}Mn_{0.9}O_2$ cathodes at 3.5 C. h) Comparison of the cycling stability of $Na_{0.7}Al_{0.1}Mn_{0.9}O_2$ and recently reported materials for AAIBs.[12,16,41–44]

hydrogen bonds during the deammoniation process. Based on these ex situ characterizations, the monkey swinging storage mechanism of $NH_4^+$ ion was further confirmed, and a schematic representation of the $NH_4^+$ ion storage mechanism in the $Na_{0.7}Al_{0.1}Mn_{0.9}O_2$ host is provided in Figure 3f.

### 2.4. Deep Understanding of the Al-Pinning Effect

It is known that the J–T distortion in the birnessite $Na_{0.7}MnO_2$ is caused by the orbital degeneracy of J–T active $Mn^{3+}$ with electronic configuration of $t_{2g}{}^3e_g{}^1$, while the non-J–T active $Mn^{4+}$ exhibits completely unoccupied $e_g$ orbitals with electronic configuration $t_{2g}{}^3e_g{}^0$ (Scheme 1b).[22] DFT calculation was then carried out to deeply understand the role of Al doping in enhancing the structural stability. Figure S15 (Supporting Information) shows the calculated projected density of states (PDOS), clearly indicating the difference in electronic state of $Mn^{3+}$ and $Mn^{4+}$. The electron (*e*) orbitals of $Mn^{4+}$ are completely vacant, whereas the J–T active $Mn^{3+}$ with an asymmetric charge distribution shows a splitting of e-orbitals into an occupied $d_{z^2}$ level and an unoccupied $d_{x^2-y^2}$ level. It can be observed that the $Mn^{3+}$ in both $Na_{0.7}MnO_2$ and $Na_{0.7}Al_{0.1}Mn_{0.9}O_2$ exhibit significant J–T distortions. Next, we conducted differential charge density analyses (**Figure** 4a,b), which show a decrease in the red region around manganese bonded with oxygen after Al doping, indicating higher electron loss and an increased valence state of Mn. Here, red and blue iso-surfaces denote electron enrichment and electro-dissipation, respectively. Bader charge analysis reveals that Al doping leads to a significant rise in Bader charge transfer value (BCTV) of per Mn atom in the unit cell from −1.239 to −1.298 e (Figure 4c). Herein, BCTV is defined as $\Delta Q = N_{Bader} - Z$, where $N_{Bader}$ is the number of electrons within the Bader volume and $Z$ is the number of valence electrons of the neutral atom. This definition only reflects the relative change in electron count compared to the neutral atom, and it is quite different with the formal chemical oxidation state. A negative $\Delta Q$ value indicates electron loss (oxidation), while a positive value indicates electron gain (reduction). As shown in Figure 4c, the increased $\Delta Q$ value implies a higher average oxidation

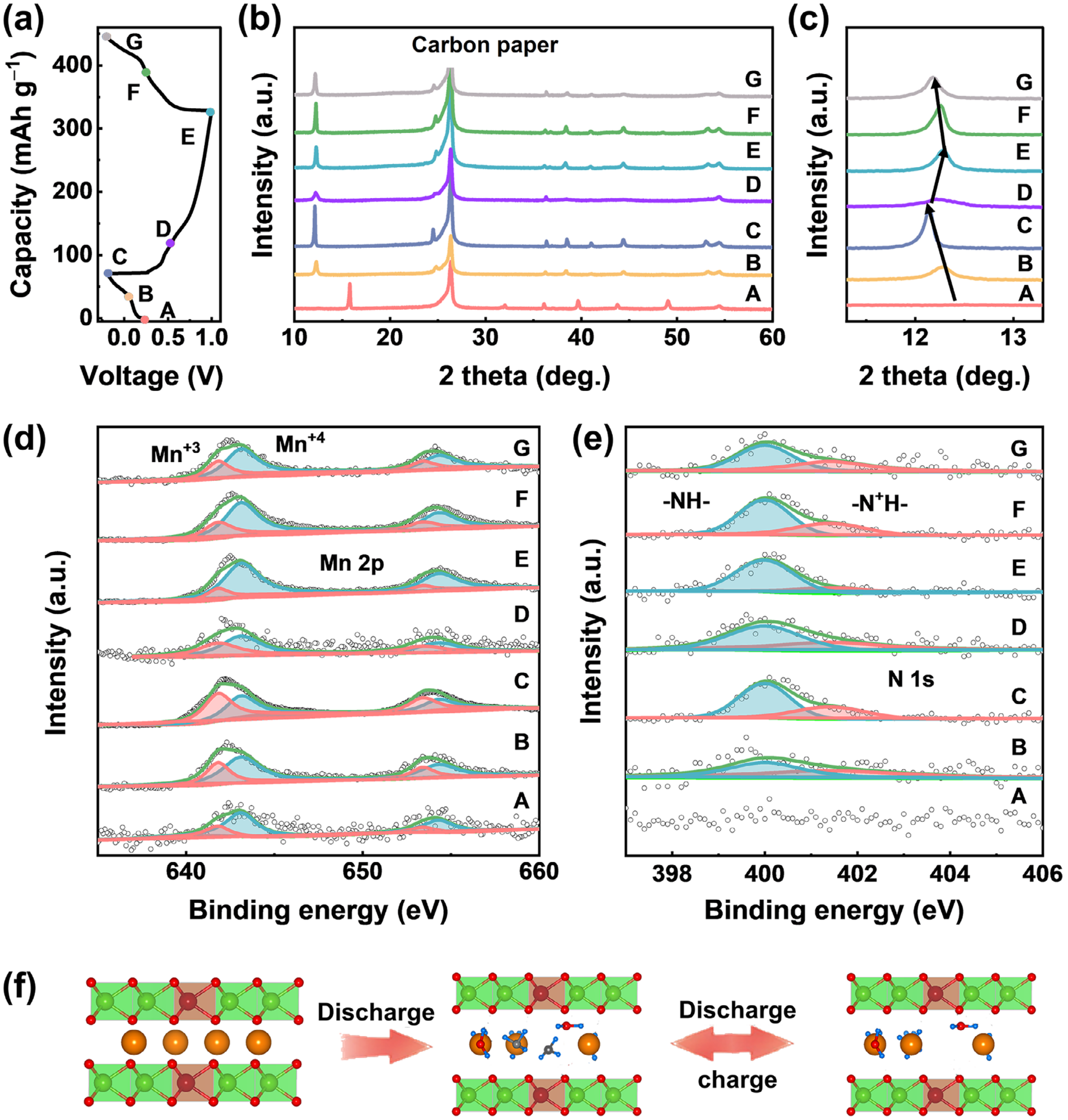

**Figure 3.** Ammonium-Ion Storage Mechanism. a) GCD curves of $Na_{0.7}Al_{0.1}Mn_{0.9}O_2$ cathode to marked out the traced states at different charged/discharged states from A to G. b,c) Ex situ XRD patterns, ex situ XPS spectra for d) Mn *2p*, e) N *1s* orbitals of the $Na_{0.7}Al_{0.1}Mn_{0.9}O_2$ cathode. f) A schematic illustrating the ammonium-ion storage mechanism in the $Na_{0.7}Al_{0.1}Mn_{0.9}O_2$ host.

state and an increased electron depletion of Mn atoms after Al doping.

Figure 4d illustrates the as-calculated density of states (DOS) for $Na_{0.7}MnO_2$ and $Na_{0.7}Al_{0.1}Mn_{0.9}O_2$ samples. It is observed that Al doping leads to a decrease in the Fermi level of $Na_{0.7}Al_{0.1}Mn_{0.9}O_2$ and an expansion of the pseudo gap. The pseudo gap reflects the covalent bonding strength within the system, and a broader pseudo gap represents stronger covalent bonding.[49] This indicates a possible strengthening of Mn—O bonds due to the hybridization of Mn(*d*)—O(*p*) and Al(*p*)—O(*p*) orbitals. The enhanced Mn—O bonds contribute to the increased structural stability of $Na_{0.7}Al_{0.1}Mn_{0.9}O_2$ upon doping. To delve deeper into the electronic and bonding characteristics of Mn, we examined the Crystal Orbital Hamiltonian Population (COHP)

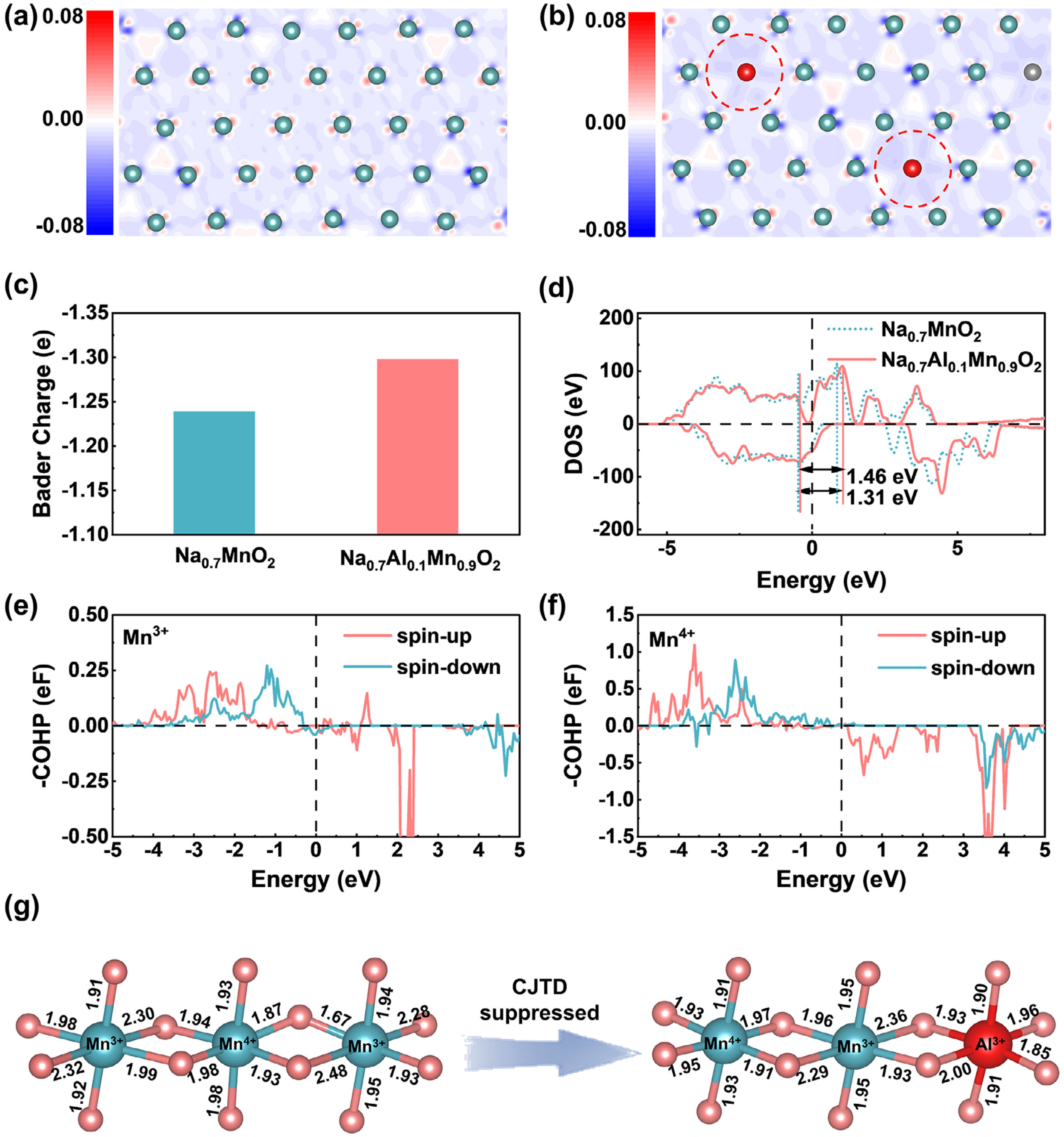

**Figure 4.** DFT calculations. Differential charge density analysis on the a) $Na_{0.7}MnO_2$ and b) $Na_{0.7}Al_{0.1}Mn_{0.9}O_2$ samples. c) Bader charge analysis. d) Total DOS plots for $Na_{0.7}MnO_2$ and $Na_{0.7}Al_{0.1}Mn_{0.9}O_2$ structures. COHP diagrams of e) $Mn^{3+}$ ions and f) $Mn^{4+}$ ions in $Na_{0.7}Al_{0.1}Mn_{0.9}O_2$. g) State of $Mn^{3+}$ octahedrons for $Na_{0.7}MnO_2$ (left) and $Na_{0.7}Al_{0.1}Mn_{0.9}O_2$ (right).

of Mn in structures with Al doping. A COHP diagram provides insights into bonding, anti-bonding, and non-bonding energy regions within a defined energy spectrum.[50] As illustrated in Figure 4e,f, the negative COHP (above $y = 0$) and the positive COHP (below $y = 0$) represent the bonding and antibonding contributions, respectively. The downshift of bonding states is clearly observed in $Mn^{4+}$ compared to that of $Mn^{3+}$. Moreover, integrated COHP (ICOHP) values are commonly used for quantitative evaluation of bonding strength. The weakened interaction between $Mn^{3+}$ and O is further confirmed by a more positive ICOHP value as −1.79 compared to −2.25 for $Mn^{4+}$—O bonds. A state with increased covalent bonding and diminished anti-bonding enhances

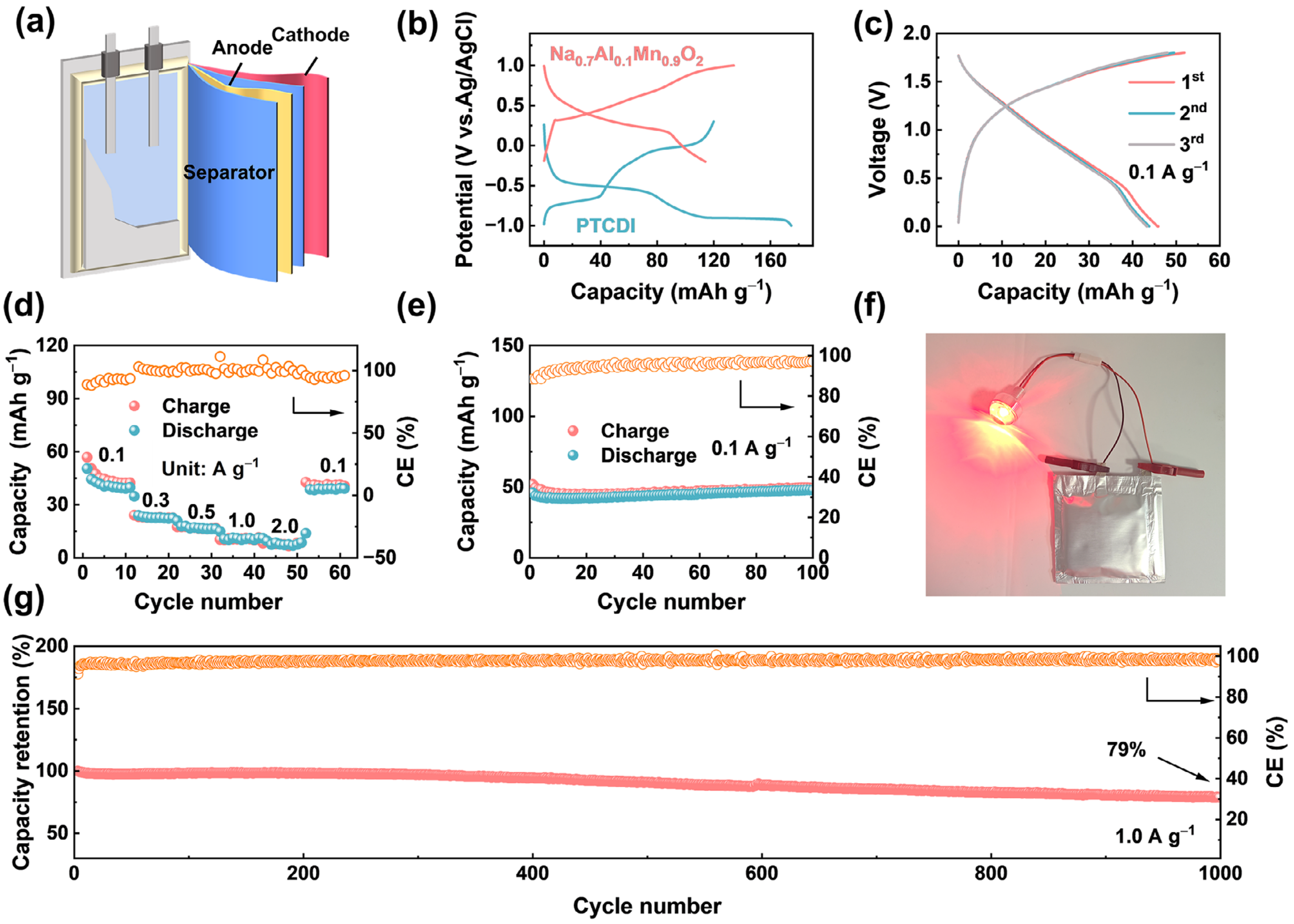

**Figure 5.** Full battery performance. a) Schematic of the assembled PTCDI//$Na_{0.7}Al_{0.1}Mn_{0.9}O_2$ full battery. b) GCD curves of activated carbon (AC)//$Na_{0.7}Al_{0.1}Mn_{0.9}O_2$ half-cell and AC//PTCDI half-cell at 100 mA g$^{-1}$. c) GCD curves, d) rate performance, and e–g) long-term stability of the PTCDI//$Na_{0.7}Al_{0.1}Mn_{0.9}O_2$ full battery at 0.1 and 1.0 A g$^{-1}$. A photograph shows that the pouch battery can to power a LED indicator.

the covalency of Mn—O bonds, subsequently decreasing Mn dissolution.

The introduction of cations (excess $Al^{3+}$ and $Al^{3+}/Mn^{3+}$ exchange) in $Na_{0.7}Al_{0.1}Mn_{0.9}O_2$ leads to the release of $Mn^{3+}$ from J–T active sites by $Al^{3+}$ ions, which destroys the symmetry of the manganese configuration. In solid state compounds, the cooperative J–T distortion (CJTD) originating from the interaction between J–T centers has a greater destructive effect on the crystal lattice than that of an individual J–T center. The addition of aluminum into the synthesized $Na_{0.7}Al_{0.1}Mn_{0.9}O_2$ breaks the correlation between individual active $Mn^{3+}$ centers and causes the $[Mn^{3+}O_6]$ octahedral extension to lack a consistent orientation and the distortions mutually offset each other instead (Figure 4g; Tables S3 and S4, Supporting Information). The $[Mn^{3+}O_6]$ octahedra in birnessite exhibit a collective J—T phenomenon, which is the interaction between the J–T distortion at individual centers. It was reported that the disordered distribution of metal cations caused by the partial substitution of manganese ions can greatly reduce the collective J–T distortion of the $[Mn^{3+}O_6]$ octahedra and the disproportionation of $Mn^{3+}$ ions.[22] The disordered distribution of cations destroys the symmetry of the manganese lattice, thereby weakening the correlation between individual J–T centers. The random distortion makes it impossible for the $[Mn^{3+}O_6]$ extension octahedra to have a uniform orientation, which easily leads to mutual offset. Therefore, the inhibition of the cooperative J–T effect is also one of the reasons for improving the electrochemical cycling stability.

### 2.5. Full Battery Performance

To evaluate the practical utility of the $Na_{0.7}Al_{0.1}Mn_{0.9}O_2$ cathode material for $NH_4^+$ ion storage, a full cell was assembled using $Na_{0.7}Al_{0.1}Mn_{0.9}O_2$ as the cathode and 3,4,9,10-perylenetetracarboxylic-diimide (PTCDI) as the anode. The schematic of this PTCDI//$Na_{0.7}Al_{0.1}Mn_{0.9}O_2$ full battery is shown in **Figure 5a**. PTCDI was selected as the anode material due to its favorable reduction potential.[32] Figure 5b indicates that PTCDI operates within a negative potential window from −1.0 to 0.2 V (vs Ag/AgCl). Furthermore, the PTCDI anode delivers a specific capacity of 125 mAh g$^{-1}$ at 0.1 A g$^{-1}$ with notable cycle stability (Figure S16, Supporting Information). The GCD curve for the PTCDI//$Na_{0.7}Al_{0.1}Mn_{0.9}O_2$ full cell, shown in Figure 5c, exhibits an average operating voltage of 0.87 V, consistent with the findings in Figure 5b, and an initial discharge specific capacity of 46 mAh $g^{-1}$ calculated based on the combined effective mass of both electrodes. The disappearance of the charge/discharge plateaus in Figure 5c should be due to the polarization effect of the full battery originated from the sluggish kinetic of the electrochemical reaction. The battery's specific capacities vary across different current densities, registering values of 40, 23, 17, 12, and 10 mAh $g^{-1}$ at 0.1, 0.3, 0.5, 1.0, and 2.0 A $g^{-1}$, respectively. When the current density returns to 0.1 A $g^{-1}$, the rate capacity recovers to 41 mAh $g^{-1}$ (Figure 5d), indicating the battery's robust reversibility. Long-term cycling tests show that the battery retains its capacity for over 100 cycles at a current density of 0.1 A $g^{-1}$, achieving a coulombic efficiency of ≈97% (Figure 5e). The first-cycle coulombic efficiency of PTCDI// $Na_{0.7}Al_{0.1}Mn_{0.9}O_2$ full battery is 88.44%, which should be due to the presence of excess $Na^+$ ions in the cathode. Remarkably, even after 1000 cycles at 1A $g^{-1}$, the capacity retention stands at 79% (Figure 5g). Especially, the as-fabricated pouch cell with the energy density of ≈40.5 Wh $kg^{-1}$ can effectively power an LED indicator (Figure 5f), suggesting its promising application potential.

## 3. Conclusion

In summary, we successfully introduce an Al pinning strategy in birnessite, which mitigates the J–T distortion of the $Mn^{3+}$ ion and simultaneously enhances the $NH_4^+$ ion diffusion kinetics. Theoretical calculations suggest that $Al^{3+}$ substitution decreases the $Mn^{3+}$ content in birnessite while elevating the oxidation state of manganese. Furthermore, the COHP illustrates that the introduction of Al enhances the covalency between Mn─O and modulates the collinear elongation or compression of $[Mn^{3+}O_6]$ octahedra. Taking advantage of these merits, the optimal $Na_{0.7}Al_{0.1}Mn_{0.9}O_2$ possesses a satisfying capacity retention of 81.6% after 5000 cycles, which surpasses that of most previously reported AAIBs. Meanwhile, Al pinning in birnessite can increase the interlayer spacing due to the regulation of $Mn^{3+}$─O/$Mn^{4+}$─O bond length and decrease the diffusion barrier for $NH_4^+$ ion in the interlayer of birnessite, leading to a high $NH_4^+$ ion diffusion coefficient of $\approx 1.58 \times 10^{-9}$ $cm^2$ $s^{-1}$. Our findings demonstrate that the Al pinning effect in birnessite can effectively suppress J–T effect and enhance the $NH_4^+$ ion diffusion kinetics simultaneously, offering the opportunities to develop robust cathode materials toward high-performance, aqueous $NH_4^+$ ion storage.

## 4. Experimental Section

*Material Synthesis*: A straightforward sol–gel process was utilized to synthesize the Al ion substituted birnessite material of $Na_{0.7}Al_xMn_{1-x}O_2$ ($x$ = 0, 0.1, 0.2, 0.3, 0.4, 0.5, and 0.6). The $x$ value represents the percentage of Al atoms relative to Mn atoms. The preparation involved dissolving the following chemicals in 50 mL of distilled water, in accordance with the stoichiometric ratio: $NaNO_3$ (0.07 mol), $Al(NO_3)_2 \cdot 9H_2O$, and $Mn(CH_3COO)_2 \cdot 4H_2O$ ($M_{Al+Mn}$ = 0.1 mol). The resulting mixture was heated to 80 °C and continuously stirred for 12 h to achieve a clear and viscous gel, followed by oven dried at 120 °C for an additional 12 h. Subsequently, the dried material was ground and then heated to 450 °C over a period of 6 h, with a heating rate of 5 °C per minute in air. After cooling to room temperature, the powder was reground, pelletized, and sintered in air at 900 °C for 15 h, with a heating rate of 5 °C per minute. Following that, the resultant material was rapidly cooled to room temperature and then stored in a glovebox purged with argon.

*Material Characterizations*: The crystal structures were studied by X-ray diffraction (XRD, Rigaku Ultima IV diffractometer with Cu Kα radiation ($\lambda$ = 1.5406 Å)). The morphology and microstructure of samples were characterized using field-emission scanning electron microscope (FESEM, QUANTA FEG250) and a transmission electron microscopy (TEM, FEI Talos F200X). Selected electron diffraction (SAED) and energy-dispersive spectrum (EDS mapping) tests were carried out, accompanied with the TEM experiments. The elemental compositions and chemical states of samples were analyzed by X-ray photoelectron spectrum (XPS, Thermo Scientific Escalab 250Xi). The chemical bonding of the samples was revealed by a Fourier transform infrared spectrometer (FTIR, Brucker TENSOR II). Inductive coupled plasma (ICP) emission spectrometer experiments were conducted on Agilent 5100 to determine the metal element concentration ratios in the prepared samples.

*Electrochemical Measurement*: The prepared $Na_{0.7}Al_xMn_{1-x}O_2$ ($x$ = 0, 0.1, and 0.2) cathode electrodes and PTCDI anode electrodes for aqueous $NH_4^+$ ion batteries were prepared by mixing the $Na_{0.7}Al_xMn_{1-x}O_2$ or PTCDI, acetylene black, and polyvinylidene fluoride (PVDF) in a mass ratio of 7:2:1, with the addition of 1-methyl-2-pyrrolidinone (NMP), followed by coating onto a carbon paper and drying under vacuum at 80 °C for 12 h. Activated carbon films were utilized as the counter anode for half battery, which were prepared by mixing the activated carbon, acetylene black and PVDF in a mass ratio of 7:2:1. Then, the slurry was coated onto a carbon paper and dried under vacuum at 80 °C for 12 h. The resulting slurry-coated carbon paper (including the $Na_{0.7}Al_xMn_{1-x}O_2$, PTCDI, and activated carbon materials) was cut into Φ10 mm electrodes. A 2.0 м $(NH_4)_2SO_4$ electrolyte solution was prepared as the electrolyte. Within the prepared electrodes, separator, electrolyte, counter electrode, Swagelok batteries were assembled in a three-electrode configuration for half battery and coin batteries for full battery to evaluate the electrochemical $NH_4^+$ ion storage performance. First, the cathode was prepared with a mass loading of $Na_{0.7}Al_xMn_{1-x}O_2$ (x = 0, 0.1, and 0.2) ≈1.5 mg $cm^{-1}$. The weight ratio of cathode ($Na_{0.7}Al_xMn_{1-x}O_2$) and anode (PTCDI) for the full devices was designed as 1.2:1 to balance the capacity difference between the cathode/anode. The total mass loading of the electroactive materials in full devices is ≈2.8 mg $cm^{-1}$. After charge/discharge cycles, the cell was disassembled for ICP-OES testing to determine the concentration of manganese species in the electrolyte. The CV and EIS tests were conducted on an electrochemical workstation (CHI660E). The GCD, GITT, and long-term cycling tests were carried out on a LAND battery test system (CT3001A).

*Theoretical Calculations*: Density functional theory (DFT) calculations were performed using the projector augmented plane-wave method within the Vienna Ab initio Simulation Package (VASP). The generalized gradient approximation (GGA) was used in the scheme of Perdew–Burke–Ernzerhof (PBE) to describe the exchange-correlation function. The cut-off energy for the plane wave was set to be 480 eV. The energy criterion was set to be $10^{-4}$ eV in the iterative solution of the Kohn–Sham equation. All the structures were relaxed until the residual forces on the atoms had declined to less than 0.05 eV $Å^{-1}$. To prevent interaction between periodic units in the vertical direction, a vacuum space of 20 Å was employed. A Monkhorst–Pack scheme with a k-points mesh of 1 × 2 × 1 was used. The diffusion barrier of adsorbed hydrogen at different adsorption sites were explored by using the Climbing image Nudge Elastic Band (CI-NEB) method.

*Electrochemical Calculations*: The diffusion coefficient $D(NH_4^+)$ of $NH_4^+$ ion can be experimentally calculated by a GITT method in terms of the following equation:

$$D = \frac{4}{\pi\tau} L^2 \left( \frac{\Delta E_s}{\Delta E_t} \right)^2 \tag{1}$$

where D is the diffusion coefficient of $NH_4^+$ ion, $\tau$ is the relaxation time of the current pulse, $L$ is the diffusion length, which is approximate to the thickness of coated slurry, and $\Delta E_s$ and $\Delta E_t$ are the voltage changes produced by the current pulse and the galvanostatic charge/discharge, respectively.

## Supporting Information

Supporting Information is available from the Wiley Online Library or from the author.

## Acknowledgements

C.C., S.Y.B., and Y.Y. contributed equally to this work. This work was financially supported by the National Natural Science Foundation of China (Grant Nos. 52171203, 52371214, 52302224, and 52271249), the National Key Research and Development Program of China (Grant No.2021YFB2400400), State Key Laboratory of Solidification Processing in NPU (Grant No.SKLSP202415), and Xi'an Talent Plan (XAYC240016). The authors are grateful for the financial support from the NCN, Poland, UMO- 2023/51/B/ST11/00504.

## Conflict of Interest

The authors declare no conflict of interest.

## Data Availability Statement

The data that support the findings of this study are available from the corresponding author upon reasonable request.

## Keywords

Al-pinning, ammonium-ion diffusion kinetics, aqueous ammonium-ion batteries, Birnessite, Jahn–Teller distortion

Received: June 29, 2025
Revised: September 19, 2025
Published online:

[1] H. Jin, D. Zhao, D. Chao, *Joule* **2025**, *9*, 101917.
[2] J. Du, Y. Zhao, X. Chu, G. Wang, C. Neumann, H. Xu, X. Li, M. Loffler, Q. Lu, J. Zhang, D. Li, J. Zou, D. Mikhailova, A. Turchanin, X. Feng, M. Yu, *Adv. Mater.* **2024**, *36*, 2313621.
[3] Y. Song, H. Qu, Z. Lao, X. Xiao, G. Lu, Y. Song, L. Nie, J. Wang, J. Yang, Y. Zhu, G. Zhou, *Adv. Mater.* **2025**, *37*, 2419271.
[4] Z. Song, L. Miao, L. Ruhlmann, Y. Lv, D. Zhu, L. Li, L. Gan, M. Liu, *Adv. Mater.* **2021**, *33*, 2104148.
[5] H. Cui, X. Gao, K. Guo, W. Liu, B. Ouyang, W. Yi, *Adv. Sci.* **2025**, *6*, 2502824.
[6] Z. Shao, L. Lin, W. Zhuang, S. Liu, P. Yang, K. Zhu, C. Li, G. Guo, W. Wang, Q. Zhang, Y. Yao, *Adv. Mater.* **2024**, *36*, 2406093.
[7] G. Liang, Y. Wang, Z. Huang, F. Mo, X. Li, Q. Yang, D. Wang, H. Li, S. Chen, C. Zhi, *Adv. Mater.* **2020**, *32*, 1907802.
[8] J. Han, A. Varzi, S. Passerini, *Angew. Chem., Int. Ed.* **2022**, *61*, 202115046.
[9] Z. Tian, V. S. Kale, S. Thomas, S. Kandambeth, I. Nadinov, Y. Wang, W. Wahyudi, Y. Lei, A. H. Emwas, M. Bonneau, O. Shekhah, O. M. Bakr, O. F. Mohammed, M. Eddaoudi, H. N. Alshareef, *Adv. Mater.* **2024**, *36*, 2409354.
[10] R. Zheng, Y. Li, H. Yu, X. Zhang, D. Yang, L. Yan, Y. Li, J. Shu, B. L. Su, *Angew. Chem., Int. Ed.* **2023**, *62*, 202301629.
[11] Z. Zhang, Y. Zhang, Z. Gao, Y. Liu, J. Gong, J. Sun, Z. Feng, T. Hu, C. Meng, *J. Energy Storage* **2024**, *83*, 110623.
[12] Y. Song, Q. Pan, H. Lv, D. Yang, Z. Qin, M. Y. Zhang, X. Sun, X. X. Liu, *Angew. Chem., Int. Ed.* **2021**, *60*, 5718.
[13] S. Mao, X. Han, Z. H. Huang, H. Li, T. Ma, *Small* **2024**, *20*, 2405592.
[14] M. Zhou, T. Wu, M. Kang, T. Cheng, H. Li, L. He, C. Lian, T. Ma, Q. Zhao, *Adv. Mater.* **2025**, *37*, 2419446.
[15] H. Lu, J. Hu, K. Zhang, Y. Zhang, B. Jiang, M. Zhang, S. Deng, J. Zhao, H. Pang, B. Xu, *Adv. Mater.* **2024**, *36*, 2408396.
[16] F. Ye, R. Pang, C. Lu, Q. Liu, Y. Wu, R. Ma, L. Hu, *Angew. Chem., Int. Ed.* **2023**, *62*, 202303480.
[17] Q. Liu, F. Ye, K. Guan, Y. Yang, H. Dong, Y. Wu, Z. Tang, L. Hu, *Adv. Energy Mater.* **2022**, *13*, 2202908.
[18] Z. Bao, C. Lu, Q. Liu, F. Ye, W. Li, Y. Zhou, L. Pan, L. Duan, H. Tang, Y. Wu, L. Hu, Z. Sun, *Nat. Commun.* **2024**, *15*, 1934.
[19] Z. Liu, R. Ma, Y. Ebina, K. Takada, T. Sasaki, *Chem. Mater.* **2007**, *19*, 6504.
[20] H. Yao, H. Yu, Y. Zheng, N. W. Li, S. Li, D. Luan, X. W. D. Lou, L. Yu, *Angew. Chem., Int. Ed.* **2023**, *62*, 202315257.
[21] Q. Liu, G. Fan, Y. Zeng, X. Zhang, D. Luan, Y. Guo, X. Gu, X. W. Lou, *Adv. Energy Mater.* **2024**, *14*, 2402743.
[22] X. Zhu, F. Meng, Q. Zhang, L. Xue, H. Zhu, S. Lan, Q. Liu, J. Zhao, Y. Zhuang, Q. Guo, B. Liu, L. Gu, X. Lu, Y. Ren, H. Xia, *Nat. Sustain.* **2020**, *4*, 392.
[23] Z. Xiao, F. Xia, L. Xu, X. Wang, J. Meng, H. Wang, X. Zhang, L. Geng, J. Wu, L. Mai, *Adv. Funct. Mater.* **2021**, *32*, 2108244.
[24] L. Zhang, C. Wang, Y. Liu, M. Ren, J. Du, A. Chen, F. Li, *Chem. Eng. J.* **2021**, *426*, 130813.
[25] Y. Zheng, H. Xie, J. Li, K. S. Hui, Z. Yu, H. Xu, D. A. Dinh, Z. Ye, C. Zha, K. N. Hui, *Adv. Energy Mater.* **2024**, *14*, 2400461.
[26] C. Wang, L. Xing, J. Vatamanu, Z. Chen, G. Lan, W. Li, K. Xu, *Nat. Commun.* **2019**, *10*, 3423.
[27] H. Chen, S. Cai, Y. Wu, W. Wang, M. Xu, S. J. Bao, *Mater. Today Energy* **2021**, *20*, 100646.
[28] J. Huang, Z. Wang, M. Hou, X. Dong, Y. Liu, Y. Wang, Y. Xia, *Nat. Commun.* **2018**, *9*, 2906.
[29] Q. Ren, Y. Yuan, S. Wang, *ACS Appl. Mater. Interfaces* **2021**, *14*, 23022.
[30] M. Peng, X. Yin, P. A. Tanner, M. G. Brik, P. Li, *Chem. Mater.* **2015**, *27*, 2938.
[31] X. Liu, W. Zuo, B. Zheng, Y. Xiang, K. Zhou, Z. Xiao, P. Shan, J. Shi, Q. Li, G. Zhong, R. Fu, Y. Yang, *Angew. Chem., Int. Ed.* **2019**, *58*, 18086.
[32] Y. Li, Y. Li, Q. Liu, Y. Liu, T. Wang, M. Cui, Y. Ding, H. Li, G. Yu, *Angew. Chem., Int. Ed.* **2024**, *63*, 202318444.
[33] W. Zhao, F. Xu, L. Liu, M. Liu, B. Weng, *Adv. Mater.* **2023**, *35*, 2308060.
[34] S. Deng, Z. Tie, F. Yue, H. Cao, M. Yao, Z. Niu, *Angew. Chem., Int. Ed.* **2022**, *61*, 202115877.
[35] L. Du, R. Zhang, H. Wang, J. Zhong, M. Xie, J. Sun, L. Kang, *Chem. Eng. J.* **2024**, *490*, 151572.
[36] S. Li, M. Xia, C. Xiao, X. Zhang, H. Yu, L. Zhang, J. Shu, *Dalton Trans.* **2021**, *50*, 6520.
[37] Z. Zhao, W. Zhang, M. Liu, D. Wang, X. Wang, L. Zheng, X. Zou, Z. Wang, D. Li, K. Huang, W. Zheng, *Energy Environ. Mater.* **2022**, *6*, 12342.
[38] H. Yu, L. Fan, H. Yan, C. Deng, L. Yan, J. Shu, Z. Wang, *Inorg. Chem. Front.* **2022**, *9*, 2001.
[39] C. Li, W. Yan, S. Liang, P. Wang, J. Wang, L. Fu, Y. Zhu, Y. Chen, Y. Wu, W. Huang, *Nanoscale Horiz.* **2019**, *4*, 991.
[40] B. Patra, S. Narayanan, S. Halder, M. Sharma, D. Sachdeva, N. Ravishankar, S. K. Pati, S. K. Jain, P. Senguttuvan, *Adv. Mater.* **2025**, *37*, 2419417.
[41] J. Han, M. Zarrabeitia, A. Mariani, M. Kuenzel, A. Mullaliu, A. Varzi, S. Passerini, *Adv. Mater.* **2022**, *34*, 2201877.

[42] Z. Tian, J. Yin, T. Guo, Z. Zhao, Y. Zhu, Y. Wang, J. Yin, Y. Zou, Y. Lei, J. Ming, O. Bakr, O. F. Mohammed, H. N. Alshareef, *Angew. Chem., Int. Ed.* **2022**, *61*, 202213757.

[43] H. Hong, J. Zhu, Y. Wang, Z. Wei, X. Guo, S. Yang, R. Zhang, H. Cui, Q. Li, D. Zhang, C. Zhi, *Adv. Mater.* **2024**, *36*, 2308210.

[44] Z. H. Huang, M. Liu, Y. Zhang, H. Li, J. Liu, Z. Wu, W. Du, H. Pan, T. Ma, *Adv. Mater.* **2025**, *37*, 2508001.

[45] W. Zuo, X. Liu, J. Qiu, D. Zhang, Z. Xiao, J. Xie, F. Ren, J. Wang, Y. Li, G. F. Ortiz, W. Wen, S. Wu, M. Wang, R. Fu, Y. Yang, *Nat. Commun.* **2021**, *12*, 4903.

[46] H. Zhang, Y. Tian, W. Wang, Z. Jian, W. Chen, *Angew. Chem., Int. Ed.* **2022**, *61*, 202204351.

[47] L. Xing, H. Chen, X. Wen, W. Zhou, K. Xiang, *J. Alloys Compd.* **2022**, *925*, 166652.

[48] S. Wang, L. Zhao, Y. Lei, Z. Li, G. Wang, *Sep. Purif. Technol.* **2024**, *329*, 125204.

[49] R. Obata, H. Sun, K. Samanta, N. A. Shahed, M. Kosugi, T. Kikkawa, A. Abdallah, K. Watanabe, T. Taniguchi, K. Suenaga, E. Saitoh, S. Maruyama, K. Hirakawa, K. D. Belashchenko, E. Y. Tsymbal, J. Haruyama, *Adv. Mater.* **2025**, *37*, 2411459.

[50] Sengupta, A. K, A. Bano, A. Ahuja, H. Lohani, S. H. Akella, P. Kumari, M. Noked, D. T. Major, S. Mitra, *Energy Storage Mater.* **2024**, *69*, 103435.